THE ASTROPHYSICAL JOURNAL, 472:398–411, 1996 November 20

THE FOOTPOINT-DRIVEN CORONAL SAUSAGE WAVE

DAVID BERGHMANS,[1] PETER DE BRUYNE, AND MARCEL GOOSSENS
Center for Plasma Astrophysics, K. U. Leuven, Celestijnenlaan 200B, B-3001 Heverlee, Belgium
Received 1996 March 3; accepted 1996 June 21

ABSTRACT

We study the excitation of MHD waves in a coronal loop as its field line footpoints are forced to follow the photospheric convective motions. By focussing on the specific case of cylindrically symmetric footpoint motions, the original problem is reduced to one in which fast waves and Alfvén waves are decoupled. This allows for a full analytical treatment of the photospheric excitation of both sausage waves and of torsional Alfvén waves. Previously, Berghmans & De Bruyne considered the case of torsional Alfvén waves. In the present paper we extend that analysis to sausage waves that are excited by radially polarized footpoint motions (e.g., typical for granules). The time-dependent solution that we obtain is written as a superposition of body and leaky eigenmodes whose excitation is easily determined from the imposed footpoint motion. This provides analytical insight into the dynamics and energetics of both impulsively and periodically driven sausage waves. In each case, we explain the time evolution of the generated waves and discuss typical "signatures" that can be looked for in numerical simulations and possibly in solar observations.

Subject headings: MHD — Sun: corona — waves

1. INTRODUCTION

Since the X-ray and UV imaging done by *Skylab* (1973), it has become clear that the solar corona is mainly structured in magnetic flux tubes, with the footpoints of the magnetic field lines tightly rooted in the dense photosphere. It is generally accepted that this line-tied magnetic loop geometry is a key ingredient toward an understanding of coronal heating. In the context of wave heating theories, one expects that impinging MHD waves are caught in the coronal part of the loop, which acts as a leaking, resonant cavity (Hollweg 1984).

A lot of work was done on sideways excitation, where one assumes a wave to impinge laterally on the loop. This problem is mathematically easier since one can include the impinging wave as a source term or boundary condition for the radial equation without having to solve the longitudinal equation explicitly. Such an impinging MHD wave must necessarily be a fast wave since Alfvén waves cannot transport energy perpendicular to the magnetic field and slow waves are negligible in the corona because of the low gas pressure. When a loop is perturbed by a pulse on its side surface, it will respond at a discrete set of fast wave frequencies characteristic of the loop's global equilibrium structure (Wright & Rickard 1995). These fast wave eigenfrequencies define what will be referred to here as the global modes. It was shown in resonant absorption theory that these global modes may locally couple to Alfvén waves when their eigenfrequency falls into the Alfvén continuum of the loop. In this process, small length scales are generated very efficiently at the coupling point. This leads to dissipation and ultimately heating of the coronal loop (see Goossens & Ruderman 1995 for a review).

However, it is important to see that sideways excitation by an externally impinging fast wave can only yield a minor contribution to the heating of a coronal loop by resonant absorption. One should recall that because of the enhanced density, the interior Alfvén speed v_{Ai} must be smaller than the exterior Alfvén speed v_{Ae}. Under these conditions, the frequency ω_f of a fast wave propagating through the coronal environment must always be higher than the Alfvén continuum $\omega_A(r)$ of the loop:

$$\omega_f = (k_x^2 + k_y^2 + k_z^2)^{1/2} v_{Ae} \geq k_z v_{Ae} > k_z v_{Ai} = \omega_A \, .$$

Therefore, only fast waves that are exponentially decaying on their way to the loop can resonantly excite Alfvén waves in the loop. This suggests that fast waves originating from within the loop must be the prime contribution. Such fast waves can be excited by, e.g., a reconnection event inside the loop (which we do not consider in this paper) or by the photospheric motions of the footpoints of the magnetic field lines.

Nevertheless, this photospheric excitation of resonant waves has been subject to criticism. One argues that typical photospheric driving frequencies and amplitudes are inadequate to generate waves that can make a relevant contribution to the heating of the corona. Because of the lack of both detailed observations and rigorous calculations, however, this criticism remains rather speculative. In fact, few investigations have been performed on how the photospheric motions drive coronal MHD waves (see, e.g., Poedts & Boyton 1996 or Čadež & Ballester 1994 for recent exceptions). Specifically, we feel that the "missing link" in wave heating scenarios by resonant absorption is the question of how resonant Alfvén waves can be indirectly driven by footpoint motions through coupling with "global modes." This problem involves the explicit solution of the wave dynamics not only in the radial direction, but also in the longitudinal direction in order to include the appropriate boundary conditions at the loop's feet. Moreover, it is advisable to study the initial value problem, since an asymptotic state may well be unattainable (Berghmans & De Bruyne 1995). As a consequence, the photospheric excitation of global modes and their subsequent coupling to resonant Alfvén waves turns out to be a difficult mathematical problem.

In an attempt to make a contribution to the solution of this problem, we start from the simplified situation of cylin-

[1] Research Assistant of the Belgian National Fund for Scientific Research.

drically symmetric perturbations ($m = 0$) in ideal, linear MHD, in which Alfvén waves and fast waves are decoupled. This has the advantage that we can study each type of wave dynamics separately, before we take their interaction (resonant absorption) into account in future studies. Berghmans & De Bruyne (1995) studied in this context how torsional deformation of a coronal loop at its footpoints excites Alfvén waves. Their simple model problem (one-dimensional wave equation) retained enough physics to study the propagation of Alfvén waves, reflections, loop resonances, and phase mixing in real space and time. Several typical timescales where derived, and it was shown that only when wave reflection at the boundaries is partial, damped back and forth running waves can build up an asymptotic state.

In this paper the model problem of Berghmans & De Bruyne (1995) is extended by allowing radially polarized excitation, which in the case of $m = 0$ means global compression (and expansion) of the coronal loop at the footpoints. This kind of photospheric driving excites the sausage wave, which is indeed the $m = 0$ member of the fast waves family. After enlisting the assumptions made, we state in § 2 the two governing equations that are decoupled thanks to the supposed cylindrical symmetry. The equation corresponding to torsionally polarized perturbations was treated in Berghmans & De Bruyne (1995) so that we can restrict the present analysis to the equation that corresponds to radially polarized perturbations. In § 3 we first transform this equation with the aid of a finite sine transform with respect to z and a Laplace transform with respect to time. This results in an inhomogeneous ordinary differential equation with respect to r. In § 4 we solve the corresponding homogeneous problem, first, as a Sturm-Liouville eigenvalue problem for the vertical wavenumber and, second, as a Schrödinger problem. Both approaches yield interesting spectral information that allows us to solve in § 5 the inhomogeneous problem and invert the finite sine transform with respect to z and the Laplace transform with respect to time. The resulting solution of the coronal, footpoint-driven sausage wave is written as a superposition of sausage eigenmodes of the loop. In § 6 we derive expressions for the kinetic energy contributions of each of these eigenmodes. These expressions turn out to be a convenient diagnostic tool in § 7, where we look at the time evolution of the resulting perturbation from impulsive and periodic footpoint motions. In each case, we explain the time evolution of the generated waves and discuss typical "signatures" that can be looked for in more realistically modeled numerical approaches and possibly in solar observations. Finally, in § 8 we summarize our results.

2. PHYSICAL MODEL

A coronal loop is modeled as a static, straight, gravitationless plasma cylinder with radius d, obeying the standard set of equations of ideal MHD. We use a cylindrical coordinate system (r, θ, z), where r represents the radial coordinate, and θ the (ignorable) poloidal coordinate. We assume the plasma to be bounded by a rigid wall condition at $r = d'$ that is sufficiently far away from the loop edge at $r = d$. This rigid wall is chosen because of mathematical simplicity but can be thought of as a consequence of interaction with nearby loops. We come back (§ 4.2) to this when taking the limit $d' \to \infty$. The z-coordinate represents length along the loop. We assume the plasma to be bounded by two rigid boundary planes: one at $z = 0$, where we impose a given footpoint motion, and the other at $z = L$, where we assume the loop is line tied. These boundary planes model the sharp transition from corona to photosphere (i.e., transition region, chromosphere, and photosphere). We will refer to these boundary planes as being the "photospheric edges" of the loop, and we implicitly assume that a disturbance initiated in the photosphere will indeed reach the corona.

The plasma is permeated by a uniform magnetic field ($\boldsymbol{B}_0 = B_0 \boldsymbol{e}_z$) and has a uniform pressure p_0, which we neglect in a low β-approximation in comparison with the magnetic pressure. Inhomogeneity of the plasma is modeled by a stepwise varying density

$$\rho_0(r) = \begin{cases} \rho_i\,, & \text{if } 0 < r < d\,, \\ \rho_e\,, & \text{if } d < r < d'\,, \end{cases} \tag{1}$$

where ρ_e denotes the exterior, coronal density (outside the loop) and ρ_i denotes the interior density (at the central axis of the loop). For simplicity, we did not take into account a z-dependence of the density. This means that our analysis is to be applied to a coronal loop with its apex lower than 1 scale height (around 100 Mm).

The plasma is being shaken by small-amplitude excitations at the footpoints of the magnetic field lines on the $z = 0$ plane. We therefore superpose linear perturbations on the previously described equilibrium. By introducing the Lagrangian displacement vector $\boldsymbol{\xi}$ as

$$\boldsymbol{v} = \frac{\partial \boldsymbol{\xi}}{\partial t}\,, \tag{2}$$

and defining the Alfvén speed as

$$v_A(r) = \sqrt{\frac{B_0^2}{\mu \rho_0(r)}}\,, \tag{3}$$

we can derive in the linear approximation the following equations

$$\left(\frac{1}{v_A^2}\frac{\partial^2}{\partial t^2} - \frac{\partial^2}{\partial z^2}\right)\xi_r = \frac{\partial}{\partial r}\left[\frac{1}{r}\frac{\partial (r\xi_r)}{\partial r} + \frac{1}{r}\frac{\partial \xi_\theta}{\partial \theta}\right], \tag{4}$$

$$\left(\frac{1}{v_A^2}\frac{\partial^2}{\partial t^2} - \frac{\partial^2}{\partial z^2}\right)\xi_\theta = \frac{1}{r}\frac{\partial}{\partial \theta}\left[\frac{1}{r}\frac{\partial (r\xi_r)}{\partial r} + \frac{1}{r}\frac{\partial \xi_\theta}{\partial \theta}\right]. \tag{5}$$

The equation for the third component of $\boldsymbol{\xi}$ describes the low-β limit of the slow mode: an anisotropic sound wave. As sound waves are not expected to yield a significant contribution to the heating of the corona (Athay & White 1978), we only consider the components in equations (4) and (5). These two equations are a coupled system of differential equations in ξ_r and ξ_θ describing coupled fast Alfvén waves. The terms on the right-hand side of these equations are proportional to gradients of total pressure:

$$P = -\frac{B_0^2}{\mu}\left[\frac{1}{r}\frac{\partial (r\xi_r)}{\partial r} + \frac{1}{r}\frac{\partial \xi_\theta}{\partial \theta}\right]. \tag{6}$$

A straightforward simplification of equations (4) and (5) can be achieved by focussing on θ-independent motions. This decouples the equations such that

$$\left(\frac{1}{v_A^2}\frac{\partial^2}{\partial t^2} - \frac{\partial^2}{\partial z^2}\right)\xi_r = \frac{\partial}{\partial r}\left[\frac{1}{r}\frac{\partial (r\xi_r)}{\partial r}\right], \tag{7}$$

$$\left(\frac{1}{v_A^2}\frac{\partial^2}{\partial t^2}-\frac{\partial^2}{\partial z^2}\right)\xi_\theta = 0\,, \tag{8}$$

while the total pressure is given by

$$P = \frac{-B_0^2}{\mu}\frac{1}{r}\frac{\partial(r\xi_r)}{\partial r}\,. \tag{9}$$

In Berghmans & De Bruyne (1995) we restricted the analysis to equation (8). The solutions of this equation are known as torsional Alfvén waves. In the present paper we solve the equation for the ξ_r component. This leads to a fully analytical solution for the footpoint-driven sausage wave in our model of coronal loops. We take all quantities in equations (7) and (8) as being nondimensionalized with respect to 1 Mm (10^6 m) for the length scales and to 1 s for the timescales. For the figures, we use the parameter set

$$L = 100\,,\quad d = 5\,,\quad d' = 50\,,$$
$$v_{Ai} = 2\,,\quad v_{Ae} = 4\,, \tag{10}$$

as typical coronal loop values, unless otherwise specified.

3. MATHEMATICAL APPROACH

Equation (7) is a partial differential equation with respect to r, z, and t, where the footpoint motions are represented by inhomogeneous boundary conditions in the z-direction:

$$\xi_r(r, z = 0, t) = R(r)T(t)\,,$$
$$\xi_r(r, z = L, t) = 0\,. \tag{11}$$

We assumed for simplicity that the dependencies on r and t of the footpoint motion are separable. The functions $T(t)$ and $R(r)$ could be matched to, for example, granule characteristics (see § 7). With the aid of the function

$$\chi(r, z, t) = \xi_r(r, z, t) - \left(1-\frac{z}{L}\right)R(r)T(t)\,, \tag{12}$$

we can include the footpoint motion as a driving term, while the boundary conditions become homogeneous:

$$\left(\frac{1}{v_A^2}\frac{\partial^2}{\partial t^2}-\frac{\partial^2}{\partial z^2}\right)\chi - \frac{\partial}{\partial r}\left[\frac{1}{r}\frac{\partial(r\chi)}{\partial r}\right] = \left(1-\frac{z}{L}\right)f(r, t)\,, \tag{13}$$

where

$$f(r, t) = T(t)\frac{\partial}{\partial r}\left[\frac{1}{r}\frac{\partial(rR)}{\partial r}\right] - \frac{R(r)}{v_A^2}\frac{\partial^2 T}{\partial t^2}\,, \tag{14}$$

and

$$\chi(z = 0) = \chi(z = L) = 0\,. \tag{15}$$

These homogeneous boundary conditions for the function χ now allow for the following sine expansion:

$$X(n) = \int_0^L \chi(z)\sin\left(\frac{n\pi}{L}z\right)dz\,, \tag{16}$$

$$\chi(z) = \frac{2}{L}\sum_{n=1}^{\infty} X(n)\sin\left(\frac{n\pi}{L}z\right). \tag{17}$$

Integration by parts yields in addition

$$\int_0^L \frac{\partial^2\xi_r}{\partial z^2}\sin\left(\frac{n\pi}{L}z\right)dz = -\left(\frac{n\pi}{L}\right)^2 X(n)\,.$$

At this stage, one might have doubts about the validity of the straight loop approximation for low-n contributions. We will come back to this in § 7.1.1.

Expanding the function $1 - z/L$ in equation (13) in a series of sines results in

$$\left(1-\frac{z}{L}\right) = \frac{2}{L}\sum_{n=1}^{\infty}\frac{L}{n\pi}\sin\left(\frac{n\pi}{L}z\right) \text{ for } z\in(0, L]\,, \tag{18}$$

where the right-hand side is convergent for all values of z except $z = 0$. This poses no difficulties since in what follows we only look for a weak solution. Using the transformation equations (17) and (18), equation (13) becomes

$$\frac{1}{v_A^2}\frac{\partial^2}{\partial t^2}X + \left(\frac{n\pi}{L}\right)^2 X - \frac{\partial}{\partial r}\left[\frac{1}{r}\frac{\partial(rX)}{\partial r}\right] = \frac{L}{n\pi}f(r, t)\,, \tag{19}$$

where X is a function of (r, n, t).

In a next step, we remove the time dependence by the following Laplace transform:

$$\hat{X}(\omega) = \int_0^\infty X(t)e^{i\omega t}\,dt\,, \tag{20}$$

$$X(t) = \frac{1}{2\pi}\int_C \hat{X}(\omega)e^{-i\omega t}\,d\omega\,, \tag{21}$$

$$\int_0^\infty \frac{\partial^2 X}{\partial t^2}e^{i\omega t}\,dt = -\omega^2\hat{X}\,, \tag{22}$$

where C is the Bromwich contour running parallel to the real axis of the ω-plane above all singularities of $\hat{X}(\omega)$. In equation (22) we assumed for simplicity that at $t = 0$

$$X(t) = 0 \quad\text{and}\quad \frac{\partial X}{\partial t} = 0 \tag{23}$$

everywhere, which avoids the need to take up initial conditions in the analysis. Applying this transform yields

$$\frac{\partial}{\partial r}\left[\frac{1}{r}\frac{\partial(r\hat{X})}{\partial r}\right] - \left[\left(\frac{n\pi}{L}\right)^2 - \frac{\omega^2}{v_A^2}\right]\hat{X} = -\left(\frac{L}{n\pi}\right)\hat{f}(r, \omega)\,, \tag{24}$$

where $\hat{X}$ is now a function of (r, n, ω). We can rewrite this equation as

$$-v_A^2(r)\left\{\frac{\partial^2}{\partial r^2}+\frac{1}{r}\frac{\partial}{\partial r}-\left[\left(\frac{n\pi}{L}\right)^2+\frac{1}{r^2}\right]\right\}\hat{X} - \omega^2\hat{X} = v_A^2(r)\left(\frac{L}{n\pi}\right)\hat{f}(r, \omega)\,, \tag{25}$$

or alternatively as

$$(A_n - \omega^2)\hat{X} = v_A^2(r)\left(\frac{L}{n\pi}\right)\hat{f}(r, \omega) \tag{26}$$

with

$$A_n\hat{X} = -\frac{v_A^2(r)}{r}\left\{\frac{\partial}{\partial r}\left(r\frac{\partial\hat{X}}{\partial r}\right) - \left[r\left(\frac{n\pi}{L}\right)^2+\frac{1}{r}\right]\hat{X}\right\}. \tag{27}$$

This problem will be solved by inverting the operator $(A_n - \omega^2)$ (§ 5). It is convenient, however, to first study the spectrum of the operator A_n.

4. THE EIGENVALUE PROBLEM

In this section we solve the problem

$$A_n X_q(r, n) = \omega_q^2(n)X_q(r, n)\,, \tag{28}$$

where the eigenfunctions X_q are subject to the Dirichlet boundary conditions: $X_q = 0$ at $r = 0$ and at $r = d'$. For later use, it is convenient to note that

$$A_{n+1} = A_n + v_A^2(r)(2n+1)\frac{\pi^2}{L^2}. \quad (29)$$

In what follows we will often drop the references to the mode number n. It is easy to check that A is self-adjoint with respect to the scalar product

$$\langle U \mid V \rangle = \int_0^{d'} U^*(r)V(r)\frac{r}{v_A^2(r)}\,dr, \quad (30)$$

where the asterisk denotes complex conjugate. In these circumstances, general theory tells us that:

1. The eigenvalues ω_q^2 are real, and
2. Eigenfunctions corresponding to different ω_q^2 are mutually orthogonal.

Rewriting equation (28) as a classical Sturm-Liouville eigenvalue problem,

$$\frac{\partial}{\partial r}\left(r\frac{\partial X_q}{\partial r}\right) - \left[r\left(\frac{n\pi}{L}\right)^2 + \frac{1}{r}\right]X_q = -\omega_q^2\frac{r}{v_A^2(r)}X_q, \quad (31)$$

we obtain the additional information that, as long as $d' < \infty$,

1. The set of eigenvalues ω_q^2 is discrete;
2. The set of eigenfunctions X_q is complete;
3. All eigenvalues ω_q^2 are strictly positive, so that all the eigenfrequencies are real.

With the help of the rescaled variable

$$r' = \sqrt{\frac{\omega_q^2}{v_{Ai}^2} - \left(\frac{n\pi}{L}\right)^2}\, r \equiv z_i(\omega_q^2)r \text{ if } 0 < r < d, \quad (32)$$

$$r' = \sqrt{\left(\frac{n\pi}{L}\right)^2 - \frac{\omega_q^2}{v_{Ae}^2}}\, r \equiv z_e(\omega_q^2)r \text{ if } d < r < d', \quad (33)$$

we can rewrite equation (31) as the Bessel equation when $r < d$,

$$\frac{\partial^2 X_q}{\partial r'^2} + \frac{1}{r'}\frac{\partial X_q}{\partial r'} + \left(1 - \frac{1}{r'^2}\right)X_q = 0, \quad (34)$$

and as the modified Bessel equation when $r > d$,

$$\frac{\partial^2 X_q}{\partial r'^2} + \frac{1}{r'}\frac{\partial X_q}{\partial r'} - \left(1 + \frac{1}{r'^2}\right)X_q = 0. \quad (35)$$

The solution inside the loop (which has to remain finite at $r = 0$) is then given by

$$J_1[z_i(\omega_q^2)r], \quad (36)$$

while imposing vanishing wave amplitude at $r = d'$ leads to the external solution

$$K_1[z_e(\omega_q^2)r]I_1[z_e(\omega_q^2)d'] - I_1[z_e(\omega_q^2)r]K_1[z_e(\omega_q^2)d']. \quad (37)$$

The condition of continuity of ξ_r and of total pressure (see eq. [9]) at $r = d$ leads to the dispersion relation

$$\begin{aligned} &z_e(\omega_q^2)J_1[z_i(\omega_q^2)d]\{K_0[z_e(\omega_q^2)d]I_1[z_e(\omega_q^2)d'] \\ &\qquad - K_1[z_e(\omega_q^2)d']I_0[z_e(\omega_q^2)d]\} \\ &= z_i(\omega_q^2)J_0[z_i(\omega_q^2)d]\{K_1[z_e(\omega_q^2)d]I_1[z_e(\omega_q^2)d'] \\ &\qquad - K_1[z_e(\omega_q^2)d']I_1[z_e(\omega_q^2)d]\}. \end{aligned} \quad (38)$$

This dispersion relation is actually a special case ($m = 0$ and $\beta = 0$) of dispersion relations found earlier by other authors (see, e.g., Cally 1986 and references therein). Each solution ω_q^2 of this equation is an eigenvalue of the operator A. The corresponding eigenfunction $X_q(r)$ is found by taking the appropriate combination of equations (36) and (37):

$$\begin{aligned} X_q(r) = {} & H(d-r)J_1[z_i(\omega_q^2)r]\{K_1[z_e(\omega_q^2)d] \\ & \times I_1[z_e(\omega_q^2)d'] - K_1[z_e(\omega_q^2)d']I_1[z_e(\omega_q^2)d]\} \\ & + H(r-d)J_1[z_i(\omega_q^2)d]\{K_1[z_e(\omega_q^2)r] \\ & \times I_1[z_e(\omega_q^2)d'] - K_1[z_e(\omega_q^2)d']I_1[z_e(\omega_q^2)r]\}, \end{aligned} \quad (39)$$

where $H(x)$ is the Heaviside step function and q ranges from 1 to ∞. The dispersion relation (eq. [38]) is transcendental and will be solved numerically. Note that starting from the eigenvalues for n, we can estimate the position of the eigenvalues for $n + 1$ from equation (29) as

$$\begin{aligned} &\omega_q^2(n) + v_{Ai}^2(2n+1)\frac{\pi^2}{L^2} \\ &\qquad < \omega_q^2(n+1) < \omega_q^2(n) + v_{Ae}^2(2n+1)\frac{\pi^2}{L^2}. \end{aligned} \quad (40)$$

These estimates were used as starting values for an iterative root-finding algorithm. The result is shown in Figure 1, where we have drawn ω_q (i.e., the positive square root of the eigenvalues ω_q^2, for different q's) as a function of n.

4.1. *Classification of Eigenmodes*

Additional insight into the spatial structure of the corresponding eigensolutions X_q can be gained by rewriting equation (35) as a Schrödinger type of equation

$$\frac{\partial^2\Phi}{\partial r^2} + \frac{1}{v_A^2(r)}[E - V(r)]\Phi = 0, \quad (41)$$

where we have defined the "wave function" $\Phi = r^{1/2}X_q(r)$, the "energy" $E = \omega_q^2$, and the "potential"

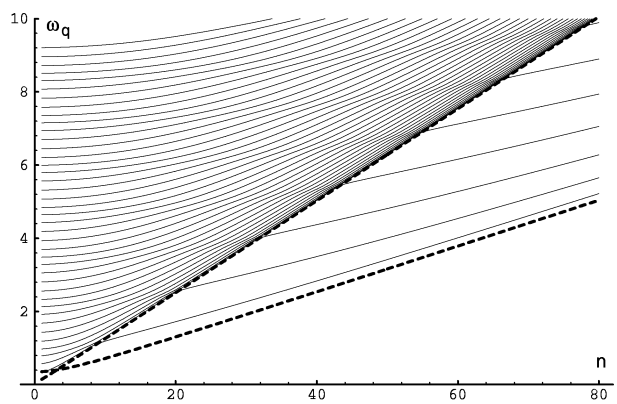

FIG. 1.—ω_q as a function of n, for q ranging from 1 (*bottom curve*) up to 40 (*top curve*). Body modes are possible between the two dashed lines (see eq. [42]). Note that the eigenfrequencies correspond to discrete n only. We have drawn lines through these discrete points for clarity.

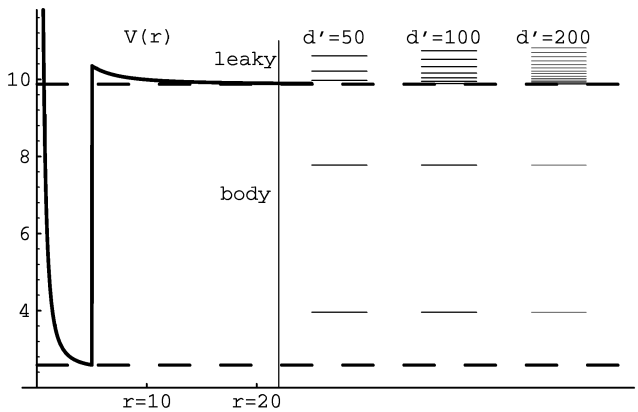

FIG. 2.—Potential $V(r)$ for $n = 25$ as a function of r (*left-hand side*) and corresponding "energy"-levels $E = \omega_q^2$ (*right-hand side*).

$$V(n, r) = v_A^2(r)\left[\left(\frac{n\pi}{L}\right)^2 + \frac{3}{4r^2}\right],$$

which is shown on the left of Figure 2 (for the case $n = 25$).

The eigenfunction X_q is oscillating in regions where $E - V(r) > 0$, but is evanescent in regions where $E - V(r) < 0$. Figure 2 shows that the stepwise profile of $v_A^2(r)$ creates a potential well inside the tube so that bound states are possible in the range

$$v_{Ai}^2\left[\left(\frac{n\pi}{L}\right)^2 + \frac{3}{4d^2}\right] < \omega_q^2 < v_{Ae}^2\left[\left(\frac{n\pi}{L}\right)^2 + \frac{3}{4d'^2}\right]. \quad (42)$$

In this range, the solutions have oscillatory behavior inside the loop and are evanescent outside the loop. This type of solution has been called "body modes." The interval (42) is depicted in Figures 1 and 2 as two dashed lines. As the height of the edge of the potential well

$$\lim_{r>d} V(r) - \lim_{r<d} V(r) = (v_{Ae}^2 - v_{Ai}^2)\left(\frac{n\pi}{L}\right)^2 \quad (43)$$

is proportional to n^2, we expect that the number of possible bound states increases when n^2 is increased. This is indeed observed in Figure 1, where we can see eigenvalues entering the region (42) for increasing n.

No solutions exist for $\omega_q^2 < v_{Ai}^2[(n\pi/L)^2 + (3/4d^2)]$, since this would correspond to a solution with exponential behavior inside and outside the loop (a so-called surface wave). Since the solution has to be zero at the boundaries, it is unavoidable that the solution peaks at $r = d$ [unless the solution is zero everywhere, which corresponds to $\omega_q^2 = v_{Ai}^2(n\pi/L)^2$]. Peaking, however, is in contradiction with continuity of total pressure [$\sim \partial(r\xi_r)/\partial r$].

Solutions with $v_{Ae}^2[(n\pi/L)^2 + (3/4d'^2)] < \omega_q^2$ oscillate not only internally, but also externally. In contrast to the body modes, which confine the wave energy inside the loop, these types of solutions radiate their energy in the surrounding coronal medium. These eigenmodes have been called leaky modes.

4.2. *The Infinite Corona Limit*

Let us investigate now what happens when taking the limit for $d' \to \infty$, so as to simulate an isolated coronal loop in an infinite medium. In the right-hand side of Figure 2 we show the effect of increasing d' on the eigenvalues. As can be expected from the analogy of our potential with those in quantum mechanical problems, the leaky mode eigenfrequencies become increasingly densely spaced, to form a continuum of radiating modes for a truly open system. The body modes, however, are hardly affected by this limit, since they vanish anyway somewhat outside the loop. These statements are of course only speculative. A proper treatment of the open system would involve a Green function approach (e.g, as in Sedláček, Adam, & Roberts 1986), with carefully chosen contour integration around the poles and branch cuts of the Green function, which then form the discrete (body modes) and continuous spectrum (leaky modes), respectively. Doing this would take us to far, but the following can be made plausible. It turns out that the analytical structure of the Green function is completely determined by its denominator, which is the same as the $d' \to \infty$ limit of our dispersion function (eq. [38]):

$$z_e(\omega_q^2)J_1[z_i(\omega_q^2)d]K_0[z_e(\omega_q^2)d] - z_i(\omega_q^2)J_0[z_i(\omega_q^2)d]K_1[z_e(\omega_q^2)d]\,. \quad (44)$$

It can be checked that this function has, apart from a discrete number of simple zeros (corresponding to the poles of the Green function), also a logarithmic branch point at $\omega_q^2 = v_{Ae}^2(n\pi/L)^2$ (i.e., $z_e = 0$) due to

$$K_1(z_e d) = \frac{1}{z_e d} + \ln(z_e d)I_1(z_e d) + \kappa_1(z_e d)\,,$$

$$K_0(z_e d) = \ln(z_e d)I_0(z_e d) + \kappa_0(z_e d)\,, \quad (45)$$

where κ_0 and κ_1 are entire functions (Erdélyi & Bateman 1953). This branch point, together with the choice of the physical Riemann sheet, dictates that the branch cut should extend from $v_{Ae}^2(n\pi/L)^2$ upwards along the real axis. Integrating along this branch cut yields the continuous spectrum contribution. The corresponding solutions for the discrete spectrum are in the limit $d' \to \infty$ given by

$$X_q^d(r) = H(d - r)J_1[z_i(\omega_q^2)r]K_1[z_e(\omega_q^2)d] + H(r - d)J_1[z_i(\omega_q^2)d]K_1[z_e(\omega_q^2)r]\,, \quad (46)$$

while for the continuous spectrum, the argument of the K_1 Bessel function becomes imaginary and we can write

$$X_q^c(r) = H(d - r)J_1[z_i(\omega_q^2)r]H_1^{(1)}[|z_e(\omega_q^2)|d] + H(r - d)J_1[z_i(\omega_q^2)d]H_1^{(1)}[|z_e(\omega_q^2)|r]\,, \quad (47)$$

where the Hankel function $H_1^{(1)}$ takes care of the outgoing wave behavior.

4.3. *Minimal Vertical Wavenumber and Frequency for Trapped Modes*

As a last item in this eigenproblem subsection, we want to derive an expression for the lowest n for which an eigenmode is trapped into the loop. That is, for each q, we want to find the n for which the corresponding eigenmode switches from leaky mode to body mode by crossing the $\omega_q^2 = v_{Ae}^2(n\pi/L)^2$ dashed line (i.e., $z_e = 0$) in Figure 1. Note that we neglect the factor $(3/4d'^2)$, since the precise value of d' has only a minor influence on body modes. For the same reason, we start from the simplified dispersion relation (eq. [44]) for $d' \to \infty$. Using equation (45) to determine the dominant behavior when $z_e \to 0$, we get

$$(z_i d)J_0[z_i d] = J_1[z_i d](z_e d)^2 \ln(z_e d) \to 0 \text{ as } z_e \to 0\,. \quad (48)$$

Since $(z_i d) \neq 0$, we get $J_0[z_i d] = 0$ or

$$d\sqrt{\frac{\omega_q^2}{v_{Ai}^2} - \left(\frac{n\pi}{L}\right)^2} = j_0^q , \tag{49}$$

where j_0^q is the qth zero of Bessel function J_0. Substituting $\omega_q^2 = v_{Ae}^2(n\pi/L)^2$ and solving for n yields an estimate $n_b(q)$ of the n-value for which the qth eigenmode becomes trapped:

$$n_b(q) = \left[\frac{L}{\pi d}\frac{j_0^q}{\sqrt{(v_{Ae}^2/v_{Ai}^2) - 1}}\right] . \tag{50}$$

A related expression for a loop of infinite length but without making the low-β approximation was derived by Roberts, Edwin, & Benz (1984). We can also eliminate n from equation (49) and $z_e = 0$ and solve for the minimal eigenfrequency that corresponds to a body mode:

$$\omega_b(q) = \frac{j_0^m}{d\sqrt{(1/v_{Ai}^2) - (1/v_{Ae}^2)}} . \tag{51}$$

For the typical coronal values specified in equation (10), we find $n_b(q = 1) = 9$ and $\omega_b(q = 1) = 1.124$. These results will be used in § 7.

5. GENERAL SOLUTION

5.1. *The Resolvent*

In this section we will solve the inhomogeneous differential equation (26). To simplify the notation, we will take the eigenfunction X_q from now on as being normalized. Using the Dirac notation

$$|X_q\rangle = X_q \quad \text{and} \quad \langle X_q| \cdot = \int_0^{d'} dr \frac{r}{v_A^2(r)} \cdot X_q ,$$

we can write the operator A as

$$A = \sum_q \omega_q^2 |X_q\rangle\langle X_q| , \tag{52}$$

and define an arbitrary function of the operator A as

$$f(A) = \sum_q f(\omega_q^2)|X_q\rangle\langle X_q| . \tag{53}$$

Specifically, by employing the function

$$f(t) = \frac{1}{t - \omega^2} ,$$

we define the "resolvent" of the operator A as

$$R_{\omega^2} \equiv \frac{1}{A - \omega^2} = \sum_q \frac{1}{\omega_q^2 - \omega^2}|X_q\rangle\langle X_q| . \tag{54}$$

It is easy to check that this resolvent operator inverts the operator $(A - \omega^2)$. Solving equation (26) is now straightforward. By operating R_{ω^2} on both sides of this equation, we obtain

$$\hat{X} = R_{\omega^2}\left[v_A^2(r)\left(\frac{L}{n\pi}\right)\hat{f}(r, \omega)\right] . \tag{55}$$

By recalling the definition of $f(r, t)$ (eq. [14]), one can rewrite this as

$$\hat{X}(r, n, \omega) = \left(\frac{L}{n\pi}\right)\sum_q \frac{\hat{T}(\omega)}{\omega_q^2 - \omega^2} X_q(r, n) \times \int_0^{d'} X_q(r, n)\left\{v_A^2(r)\frac{\partial}{\partial r}\left[\frac{1}{r}\frac{\partial(rR)}{\partial r}\right] + \omega^2 R(r)\right\} r\, dr . \tag{56}$$

In a lengthy but straightforward derivation, the r derivatives on $R(r)$ can be removed by partial integration. This simplifies the expression to

$$\hat{X}(r, n, \omega) = -\left(\frac{L}{n\pi}\right)R(r)\hat{T}(\omega) + \left(\frac{n\pi}{L}\right)\sum_q \frac{\hat{T}(\omega)}{\omega_q^2 - \omega^2} \times \left[\int_0^{d'} X_q(r, n)R(r) r\, dr\right] X_q(r, n) . \tag{57}$$

5.2. *Inversion of Transformations*

We now want to invert the Laplace transform with respect to time and the sine transform with respect to z. The Laplace inversion of the first term of equation (57) is straightforward:

$$-\left(\frac{L}{n\pi}\right)R(r)\hat{T}(\omega) \rightarrow -\left(\frac{L}{n\pi}\right)R(r)T(t) .$$

To perform the Laplace inversion of the second term of equation (57), we first note that the complete ω-dependence is contained in the factor

$$\frac{\hat{T}(\omega)}{\omega_q^2 - \omega^2} . \tag{58}$$

Second, one should remember the well-known inversions

$$\frac{1}{\omega_q^2 - \omega^2} \rightarrow \frac{\sin(\omega_q t)}{\omega_q} , \tag{59}$$

$$\hat{f}_1(\omega)\hat{f}_2(\omega) \rightarrow \int_0^t f_1(t - \tau)f_2(\tau)d\tau . \tag{60}$$

Combining these two results allows us to invert

$$\frac{\hat{T}(\omega)}{\omega_q^2 - \omega^2} \rightarrow \frac{1}{\omega_q}\int_0^t \sin\omega_q(t - \tau)T(\tau)d\tau . \tag{61}$$

Plugging this result into equation (57) yields

$$X(r, n, t) = -\left(\frac{L}{n\pi}\right)R(r)T(t) + \sum_{q=1}^{\infty}\langle X_q|v_A^2(r)R(r)\rangle \times \left[\frac{n\pi}{\omega_q L}\sin(\omega_q t), T(t)\right] X_q(r, n) , \tag{62}$$

where we used the scalar product

$$\langle X_q|v_A^2(r)R(r)\rangle = \int_0^{d'} X_q(r, n)R(r) r\, dr \tag{63}$$

and the time convolution

$$\left[\frac{n\pi}{\omega_q L}\sin(\omega_q t), T(t)\right] = \frac{n\pi}{\omega_q L}\int_0^t \sin\omega_q(t - \tau)T(\tau)d\tau . \tag{64}$$

By recalling the definition of χ and the transform equation (17), we can now reconstruct the displacement ξ_r as a function of r, z, and t:

$$\xi_r(r, z, t) = \chi(r, z, t) + \left(1 - \frac{z}{L}\right)R(r)T(t) , = \frac{2}{L}\sum_{n=1}^{\infty} X(r, n, t)\sin\left(\frac{n\pi}{L} z\right) + \left(1 - \frac{z}{L}\right)R(r)T(t) . \tag{65}$$

This gives

$$\xi_r(r, z, t) = \sum_{n=1}^{\infty} \sum_{q=1}^{\infty} \langle X_q | v_A^2(r) R(r) \rangle \times \left[\frac{n\pi}{\omega_q L} \sin(\omega_q t), T(t) \right] S_{q,n}(r, z) + R(r)T(t) \times \left[\left(1 - \frac{z}{L}\right) - \frac{2}{L} \sum_{n=1}^{\infty} \frac{L}{n\pi} \sin\left(\frac{n\pi}{L} z\right) \right], \quad (66)$$

where we defined the sausage eigenmode

$$S_{q,n}(r, z) = \frac{2}{L} \sin\left(\frac{n\pi}{L} z\right) X_q(r, n) . \quad (67)$$

As a result of equation (18), the second term of equation (66) equals zero for all values of $z > 0$. However, when $z = 0$, the second term equals $R(r)T(t)$, which is indeed the imposed footpoint motion, while the first term of equation (66) [being a superposition of terms proportional to $\sin(n\pi z/L)$] becomes zero. The solution can thus be written as

$$\xi_r(r, z, t) = \sum_{n=1}^{\infty} \sum_{q=1}^{\infty} \langle X_q | v_A^2(r) R(r) \rangle \left[\frac{n\pi}{\omega_q L} \sin(\omega_q t), T(t) \right] \times S_{q,n}(r, z) + R(r)T(t)\delta_{z0} . \quad (68)$$

Equation (68) gives a description of the generation by footpoint motions of sausage waves in a coronal loop as it was modeled in § 2. The solution is written as a superposition of sausage eigenmodes $S_{q,n}(r, z)$ whose excitation is determined by the time dependence $T(t)$ of the footpoint motion through convolution (64) and by the spatial dependence of the footpoint motion through the scalar product (63). In addition, a term $R(r)T(t)\delta_{z0}$ appears for reasons of convergence, which is only nonzero at $z = 0$. It is important to note that the procedure that led to the solution (68) is independent of the precise choice of the Alfvén profile $v_A(r)$. Indeed, any other profile would still lead to a self-adjoint operator (27), which is the basis of our analysis. Our choice of a step profile has the advantage of being analytically tractable, while other profiles would require a numerical procedure to determine the eigenfunctions.

6. KINETIC ENERGY

From the solution (68), one can construct the total kinetic energy $E(t)$ in the system:

$$E(t) = 2\pi \int_0^L dz \int_0^{d'} r\, dr\, \frac{1}{2} \rho_0(r) \left[\frac{\partial \xi_r(r, z, t)}{\partial t} \right]^2 . \quad (69)$$

Since

$$\int_0^L dz \int_0^{d'} \rho_0(r) r\, dr S_{q,n}(r, z) S_{q',n'}(r, z) = \frac{2B_0^2}{L\mu} \delta_{q,q'} \delta_{n,n'} , \quad (70)$$

one can rewrite equation (69) as

$$E(t) = C \sum_{n=1}^{\infty} \sum_{q=1}^{\infty} E_{q,n}(t) , \quad (71)$$

where

$$E_{q,n}(t) = |\langle X_q | v_A^2 R \rangle|^2 \left(\frac{n\pi}{L}\right)^2 \left\{ \int_0^t \cos[\omega_q(t - \tau)] T(\tau) d\tau \right\}^2 , \quad (72)$$

and $C = 4\pi B_0^2/\mu L$. Of course, each term of equation (71) is just the kinetic energy contribution $E_{q,n}(t)$ of each eigenmode $S_{q,n}(r, z)$ (scaled by a constant factor C). In what follows, we will also use the time-averaged kinetic energy contributions

$$\langle E_{q,n} \rangle = \frac{1}{P} \int_P^{2P} E_{q,n}(t) dt , \quad (73)$$

where P is a period longer than any period of the system or of the footpoint motion.

Although we took $d' \gg d$, the wave behavior in the loop might be influenced by the outer boundary d' for times later than $(d' - d)/v_{Ae}$, which is the time to travel from the boundary to the loop. In general, this influence is small since the amplitude of a wave expanding in two dimensions decreases as $R^{-1/2}$, where R is the distance traveled. As mentioned above, the reflections on d' can be seen as the influence of nearby loops. However, if one wants to investigate the asymptotic state $t \to \infty$, these contributions might accumulate, leading to spurious standing waves in the r-direction. These complications can be avoided by retaining only those terms in equation (71) that correspond to body modes. Indeed, for a truly infinite medium (see § 4.2), the leaky modes will radiate most of their energy in a finite time, leaving only the contribution of the body modes as $t \to \infty$. In this sense, we can estimate the energy confinement of the loop in an infinite corona by the ratio

$$\mathrm{ECR} = \frac{\sum_{\mathrm{body}} \langle E_{q,n} \rangle}{\sum_{\mathrm{body+leaky}} \langle E_{q,n} \rangle} . \quad (74)$$

7. APPLICATIONS

In this section we will use equation (68) to visualize the behavior of the sausage wave under varying conditions. We again take the typical parameter set (eq. [10]) and look at the influence of the functions $R(r)$ and $T(t)$, which characterize the footpoint motion (eq. [11]). Because of the imposed axial symmetry ($m = 0$), the footpoint motion always has the topology of a ring. This is not a shortcoming or restriction of our analysis. It is a direct consequence of the fact that a ringlike footpoint motion (i.e., $m = 0$) is the only Fourier component [$\exp(im\theta)$] generating the sausage waves. In this sense, an external excitation that is concentrated near a point rather than a ring will have a $m = 0$ component that excites sausage waves.

For the numerical calculations, we replace the double infinite sum in equation (68) by

$$\sum_{n=1}^{N} \sum_{q=1}^{Q} . \quad (75)$$

The consequence of this approximation is that features in the solution with a typical scale of $O(L/N)$ in the z-direction and a typical scale of $O(d'/Q)$ in the x-direction might not be adequately represented. For example, in the initial stage (small t), the solution is zero everywhere except in a narrow region $z \in [0, tv_A]$. This causes spurious oscillations until $t \gg O(L/v_A N)$. To minimize these problems, we took N and Q typically as large as 250 and 75, respectively. The solution (68) together with the approximation (75) was used to produce a time sequence of pictures in the following situations.

7.1. *Pulsewise Driving*

In a first approach, we want to study footpoint motions with a time dependence

$$T(t) = H(t)\left[\frac{1}{4}\left(\frac{t}{t_0}\right)^2 \exp\left(2 - \frac{t}{t_0}\right)\right], \qquad (76)$$

which is chosen in order to simulate giving an instant "kick" (e.g., an exploding granule) at the loop's feet. This time dependence is in agreement with the absence of initial conditions (23). The maximum amplitude 1 is reached when $t = 2t_0$. In what follows, we (arbitrarily) take $t_0 = 0.25$.

7.1.1. *An External Pulse*

As a kind of a test case, we first want to consider driving outside the loop:

$$R(r) = H(r - 15)H(20 - r)\,. \qquad (77)$$

In Figure 3 we have drawn the lower part (up to $z = 35$) of the corona. In Figure 3*a* we show the wave front at $t = 1$. We can see that the wave front has expanded spherically over distance: $v_{Ae}t = 4$. At $t = 2.5$ (Fig. 3*b*), a negative wake (region 2) has developed behind the expanding positive front (region 1). Such a negative wake is typical for wave fronts expanding in two dimensions (see, e.g., Morse & Feshbach, 1953). At $t = 5.5$ (Fig. 3*c*), the wave front has encountered the loop edge and is partially refracted into the loop (region 3), while the rest is reflected back into the corona with reversed amplitude (region 4). In Figure 3*d* we see the original spherically expanding wave front (1) and its wake (2), the reflected wave front (4), the reflected wake (5), the refracted wave front (3), and the refracted wake (6). The remaining two regions (7 and 8) are coming "from the other side" of the loop axis and need some explanation. Because of the cylindrical symmetry, we have actually perturbed the photosphere at a ring around the loop axis. The wave front that originated at the opposite side of this ring was originally pointing outward ($\xi_r > 0$), but when crossing the loop axis, this became pointing inward ($\xi_r < 0$) and thus gave rise to the negative wave front (7). The region (8) is just the companion wake to the wave front (7). Equivalently, the regions (7) and (8) can be seen as the reflections of (3) and (6) on the loop axis $r = 0$, which needs to remain unperturbed in a cylindrically symmetric situation.

As the wave front (7) and its wake (8) travel almost perpendicularly to the loop edge, they reescape into the outer corona rather than traveling along the loop. The effect in the long run is that almost nothing of the original pulse

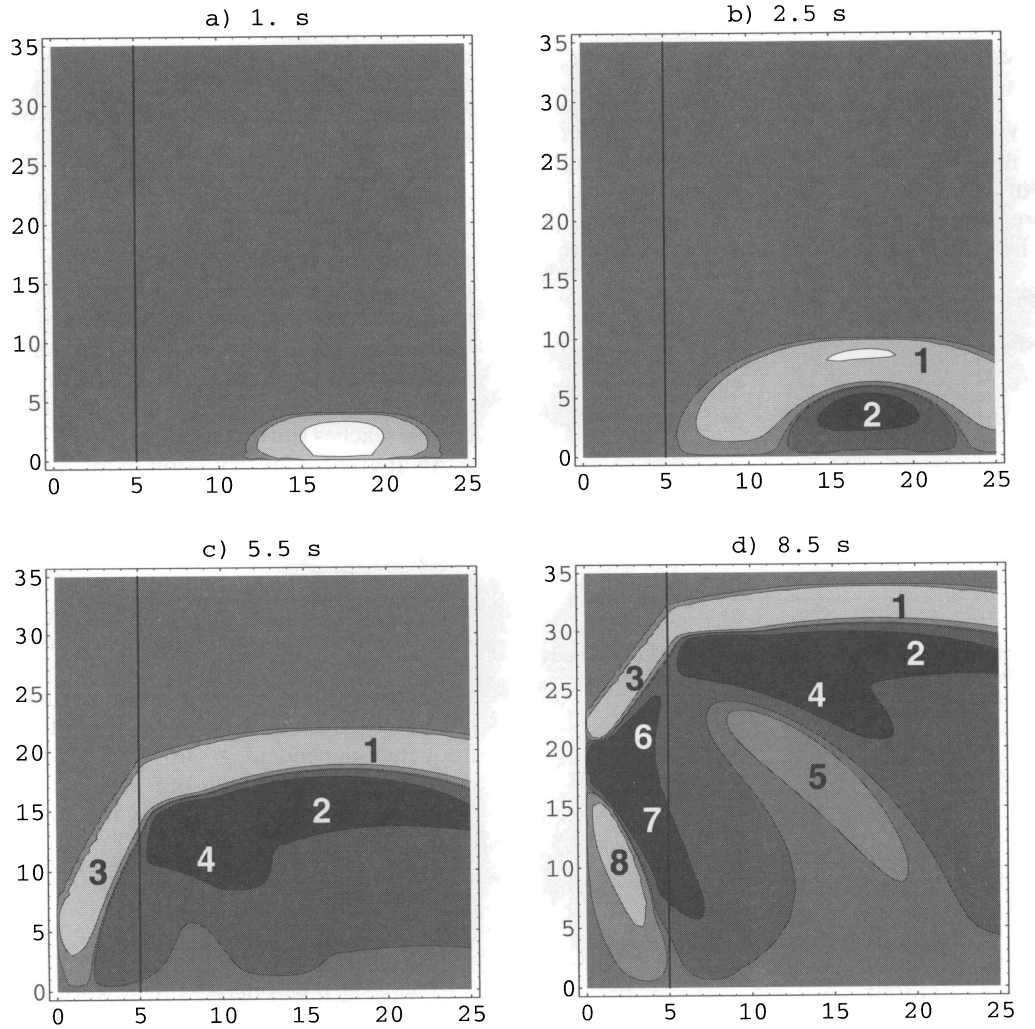

FIG. 3.—Contour plots at different times of the wave amplitude due to an external pulse as a function of height (*vertical axis*) and radius (*horizontal axis*). The contours are chosen at $\{\pm 0.5, \pm 0.05, \pm 0.005\}$, where light regions are positive (radially outward, expansion) and dark regions are negative (radially inward, compression). The vertical line at $r = 5$ represents the loop edge.

energy is captured by the loop. This can also be understood from the following argument. As we stated above, the only modes that can confine energy to the loop for $t \to \infty$ are the body modes. Since these modes are evanescent for $r > d$, the corresponding scalar products (63) [with $R(r)$ which is only nonzero for $r \gg d$] are very small. This is indeed confirmed in Figures 4 and 5, where we plotted the time-averaged kinetic energy (up to a factor C) of the body modes and the leaky modes, respectively, as a function of the corresponding eigenfrequency. By far the largest contribution comes from the leaky modes, while the body modes are (almost) not excited. This means that the loop is unable to capture any significant amount of energy. We find an energy confinement ratio of only ECR = 1%.

We also calculated the contribution from the lowest n-modes to the total kinetic energy. As stated in § 3, these modes, which have a vertical wavelength comparable to the loop length, might be heavily influenced by the assumption of a straight loop instead of a curved one. It turns out, however, that in the present case the lowest n-modes (say $n = 1$ to 4) contribute only 6.41% of the total kinetic energy such that the "rectification" of the loop seems a posteriori a reasonable approach.

7.1.2. *An Internal Pulse*

A completely different picture is obtained if we impose as footpoint motion a pulse *inside* the loop,

$$R(r) = H(r - 2)H(4.5 - r)\,, \tag{78}$$

while keeping the same "kick" time dependence (eq. [76]).

Figure 6*a* shows the wave front at $t = 1.2$. At this time, the footpoint motion is already beyond its maximal amplitude (which occurs at $t = 0.5$) and is exponentially decaying again. Therefore, the brightest region in Figure 6*a* is detached from the bottom. Because of a change in the horizontal scale, the wave front appears as a flat dish rather than a sphere. In particular, one sees the wave front that propagates straight up with a speed $v_{Ai} = 2$ (labeled 1) and the wave front that has left the loop and therefore expands rapidly with a speed $v_{Ae} = 4$ (labeled 2).

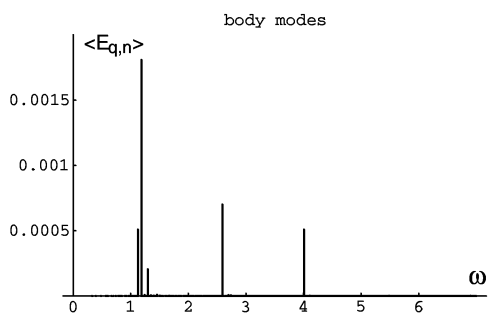

FIG. 4.—Time-averaged kinetic energy contribution $\langle E_{q,n} \rangle$ of the body modes due to an external pulse.

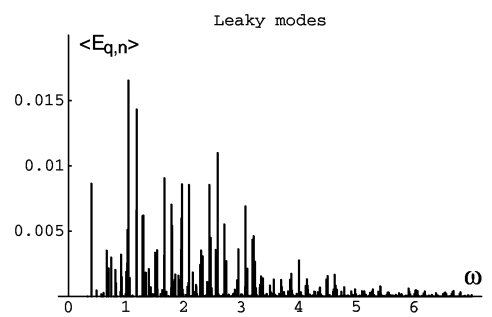

FIG. 5.—Time-averaged kinetic energy contribution $\langle E_{q,n} \rangle$ of the leaky modes due to an external pulse.

In Figure 6*b* ($t = 1.8$) a new dark (i.e., negative amplitude) spot emerges at the bottom of the loop. This spot is the wake of wave front 1, as encountered in the previous case. In Figure 6*c* ($t = 2.4$) we can see that this negative region has grown quickly. This is because the wake is reinforced by the initially positive wave front "coming from the other side of the loop axis," which became negative on crossing the axis. To trace the motion in subsequent pictures of the negative wave front that is bursting out of the loop, we have added a point labeled 3. The upward rising wave front 1 has reached a height $z = 2.4 v_{Ai} = 4.8$. Nevertheless, one can see that around $r = 4.5$ some perturbation is reentering the loop at greater heights. In fact, the wave front 2 is turning back into the loop. This behavior is caused by the imposed boundary conditions at the loop edge, which demand a smooth transition of the wave fronts inside and outside the loop.

In Figure 6*d* ($t = 3.4$) the directly uprising wave front 1 is being caught up by the reentry wave front 2. Meanwhile, a new positive region emerges (Fig. 6*d*, *bottom left corner*), because of the wake originating at the other side of the loop. After some time (at $t = 6$), this region becomes the large positive wave front that we labeled 4 in Figure 6*e*. In this figure one can see that the negative wave front 3 in its turn is turning back into the loop, thereby eating the preceding positive region from the back.

The result is in Figure 6*f* ($t = 8.8$). Ahead of the directly uprising wave front 1, there is an oscillating pattern caused by the reentry of the wave fronts 2 and 3. Behind the directly uprising wave front 1, one gets a complicated picture of alternating positive and negative regions of increasing vertical wavelength, caused by multiple reflections of the wave front and its wake. As time progresses, the reentry effect ahead of wave front 1 and the multiple reflection behind it go on for some time until the first perturbation reaches the other side $z = L$.

An analytical investigation of this behavior is impeded by the finite sine transform (eq. [17]) that enabled us to study the excitation of eigenmodes, but which is less convenient to study the evolution in terms of propagating wave fronts. However, Roberts, Edwin, & Benz (1984) noted the close analogy between sausage modes in coronal loops and Pekeris waves in oceanography. This was very fortunate since it allowed them to use the analytical work for Pekeris waves to explain the typical signature of an impulsively generated sausage wave in an infinite loop in terms of a frequency-dependent group velocity. It turns out that this close analogy persists in our line-tied loop with footpoint-driven sausage waves. To show this, we let the perturbation evolve from $t = 8.6$ (i.e., Fig. 6*f*) up to $t = L/v_{Ae} = 25$ (time at which $z = L$ is reached). In Figure 7 we show a crosscut of this situation for a fixed radius ($r = 4.4$), which yields the amplitude as a function of height.

The result is a typical signature of an impulsively generated wave as it was derived by Pekeris (1948) for a two-layer ocean model. The reentry wave fronts form what Pekeris called the periodic phase, while the subsequent oscillations due to multiple reflections were called the quasi-periodic phase. The final decay was called the Airy phase. The small

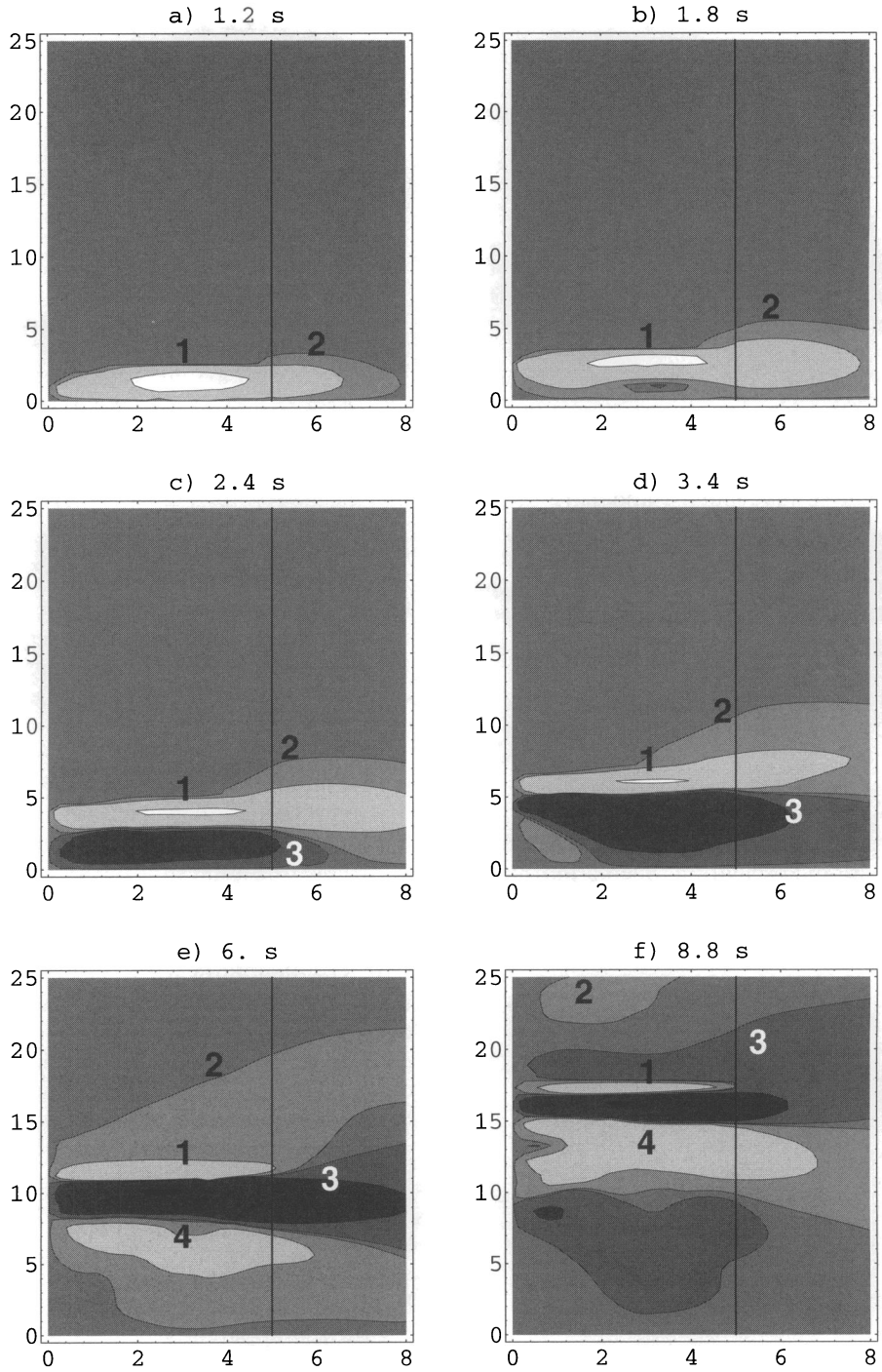

FIG. 6.—Contour plots (as in Fig. 3) of the amplitude due to an internal pulse

oscillation superposed on the periodic phase is a numerical artifact caused by the truncation of the sum in equation (68). The spikes seen in the decay phase are probably due to ongoing reflections.

Once the periodic phase has reached $z = L$, reflection occurs and the "head" of the Pekeris wave is reflected downwards, superposed on its tail. The following pictures in the time series of Figure 6 therefore quickly become uninterpretable. Thanks to the equations (71) and (74), however, we can still draw some conclusions for large t. In Figures 8 and 9 we depict the time-averaged kinetic energy contributions (up to a constant factor C) of the leaky and body modes due to the internal pulse. Contrary to the former case of an external pulse, the largest contributions are now clearly coming from the body modes, which start at the lowest body mode eigenfrequency derived in § 4.3 [$\omega_b(q = 1) = 1.124$, which corresponds to $n_b(q = 1) = 9$]. Only below this frequency $\omega_b(q = 1)$ are there significant leaky mode contributions. This means that in the long run, when leaky modes have died out, the perturbation has at least nine nodes in the z-direction.

The largest kinetic energies for the body modes are seen in the frequency range 1.1–4.5, which corresponds to timescales (half a period) of 0.7–2.9 s. It is interesting to note that fluctuation timescales of 0.5–3.0 s have indeed been observed for twenty years now by a large number of authors

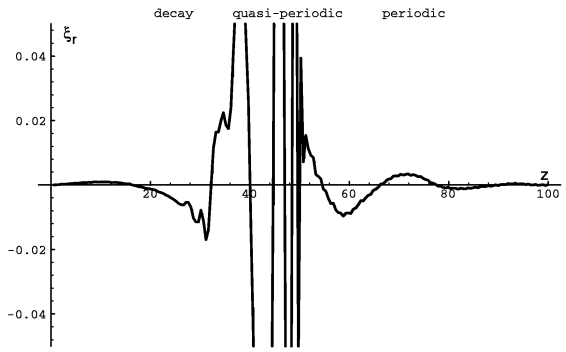

FIG. 7.—Wave amplitude at $t = 25$ due to an internal pulse as a function of height z for a fixed radius $r = 4.4$.

in solar radio bursts, microwave bursts, and hard X-ray bursts (see, e.g., Ren-Yang, Sheng-Zhen, & Xiao-Cong 1990 and references therein). It thus seems that, as instrumentation is refined, it might become possible to link the observations with the theoretical framework presented here. If successful, this might lead to MHD spectroscopy of coronal loops.

Since predominantly body modes are excited, we can expect a large energy confinement ratio, which turns out to be ECR = 94%.

7.2. *Periodic Driving*

In this subsection we want to turn to the case of driving the loop's feet with a periodic oscillation. Such a footpoint motion could be generated, for example, by a subphotospheric wave. We consider a harmonic footpoint motion $\sin(\omega_d t)$ that is preceded by a t^2 growth as in equation (76), to remain consistent with the initial conditions (23), and that dies out after a time τ_c:

$$T(t) = \begin{cases} \frac{1}{4} H(t) \left(\frac{t}{t_0}\right)^2 \exp\left(2 - \frac{t}{t_0}\right), & \text{if } t < 2t_0 , \\ \sin(\omega_d t) , & \text{if } 2t_0 < t < \tau_c , \\ 0 , & \text{if } \tau_c < t , \end{cases} \tag{79}$$

where t_0 is taken to be $\pi/2\omega_d$ to guarantee a smooth fitting (continuous amplitude [= 1] and continuous first derivative [= 0]). We also assume that $\omega_d \tau_c$ is an integer multiple of 2π (i.e., $\tau_c = m2\pi/\omega_d$) to avoid an abrupt end of the footpoint driving. The radial dependence is kept the same as in the previous case:

$$R(r) = H(r - 2)H(4.5 - r) . \tag{80}$$

From what we have seen above, it should be no surprise that driving at the loop's feet with a periodically oscillating footpoint motion (which can be seen as a sequence of alternating pulses) results in a complicated wave pattern that is hard to interpret. To keep things tractable, we split the discussion into the following time intervals.

7.2.1. *Initial Stage*: $t < L/v_{Ae}$

In Figure 10 we show a time sequence of pictures for driving with a frequency $\omega_d = 1$, which is close to the leaky mode $\omega_{q=2}(n = 7) = 1.0003$. Instead of trying to interpret the whole evolution in terms of propagating and reflecting wave fronts and trailing wakes, we want to focus on two observations:

1. The first outward (light) and inward (dark) phases reach a height of $z \sim 6$, 10, 12, respectively, before they detach from the bottom $z = 0$. For later times, this number goes up to $z \sim 16$, which is much more than what can be expected ($z = v_{Ai} \Delta t = 2\pi$) from the time between two nodes of the footpoint oscillation ($\Delta t = \pi$).
2. Once detached from the bottom, the leading wave front decays while propagating upwards. For longer time sequences, the same narrowing of the following waves up to disappearance is observed.

As far as the first observation stated is concerned, we hypothesize that, for example, the first negative phase in Figure 10*b* apparently reaches a height $z = 10$, instead of $z = 2\pi$, because it is headed by the wake of the first positive phase and the "reflection" of the first positive phase on the loop axis (as in Fig. 6*c*). The same mechanism is probably operating for later phases as well.

Concerning the second observation, one could argue that this is due to the two-dimensional expansion of the wave front. We think that a more wave-destructive mechanism is at work inside the loop. Let us look at the upward propagating train of alternating inward or outward phases as a series of pulses. As in the case of pulsewise driving, a part of a specific pulse bursts through the loop edge and reenters somewhat ahead of the directly uprising wave front superposed on the preceding pulse, which has the opposite sign. This preceding pulse therefore diminishes in amplitude. Analogously, our specific pulse is hit from the back by the reentry wave front of the trailing pulse and thus also diminishes in amplitude. Since each of the pulses is somewhat

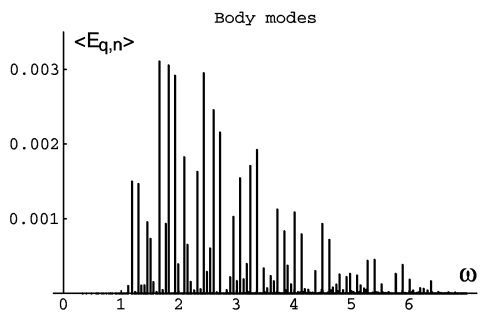

FIG. 8.—Time-averaged kinetic energy contribution $\langle E_{q,n} \rangle$ of the body modes due to an internal pulse.

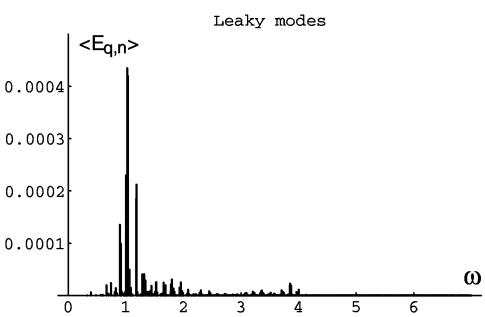

FIG. 9.—Time-averaged kinetic energy contribution $\langle E_{q,n} \rangle$ of the leaky modes due to an internal pulse.

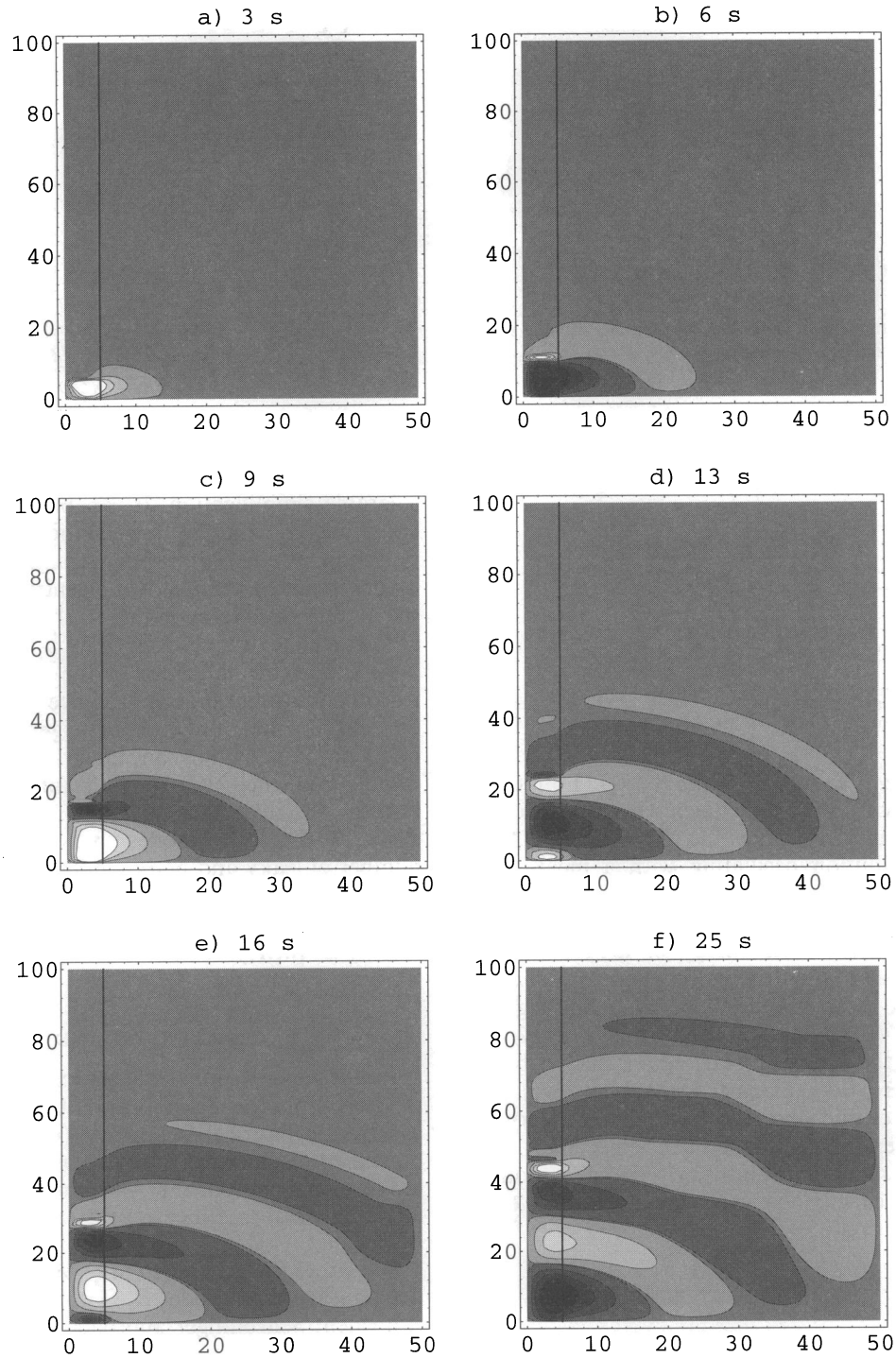

FIG. 10.—Wave amplitude as a function of height (*vertical axis*) and radius (*horizontal axis*) due to harmonic footpoint driving with a frequency $\omega_d = 1$

larger than its predecessor pulse (since this pulse has been expanding for a longer time), one pulse after the other is effectively destroyed. In Figure 11 we show a crosscut for a fixed radius $r = 4$ of the situation in Figure 10, at time $t = 25$. At this time, the rising wave train has reached a height $z = 50$. Since we drive with a frequency $\omega_d = 1$, one would expect to see $25/\pi \sim 8$ alternating positive and negative phases between $z = 0$ and $z = 50$. Instead, one sees only four phases and a small hump on its way to disappear. Although oscillations are disappearing one after the other, the eigenmode $q = 2$, $n = 7$, whose frequency we are driving with, is being build up. Indeed, in Figure 11 we see that the first three "pulses" reach from $z = 0$ to $z = 42$, giving an average pulse width of $\Delta z = 13$, which means that seven of these pulses would fit in the length of the loop ($L = 100$). This is indeed the n-number of the eigenmode whose frequency we are driving with.

7.2.2. *Ongoing Driving*: $t < \tau_c$

Let us investigate the influence of the frequency ω_d on the excitation of each sausage eigenmode $S_{q,n}$ in more detail. The driving frequency ω_d enters equation (72) via the integral over τ, which for the present case of $T(t) = \sin(\omega_d t)$ (for simplicity we forget about the initial stage) can be easily

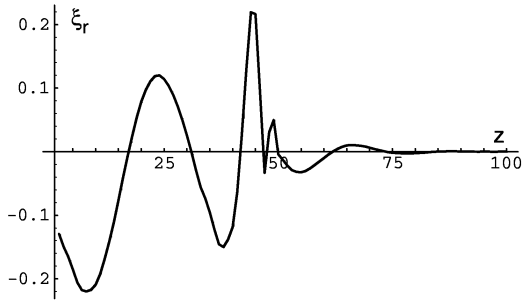

FIG. 11.—Wave amplitude at $t = 25$ due to periodic driving with $\omega_d = 1$ as a function of height, for a fixed radius $r = 4$.

integrated analytically. This results in

$$E_{q,n}(t) = |\langle X_q | v_A^2 R\rangle|^2 \left(\frac{n\pi}{L}\right)^2 \times \left[\omega_d \frac{\cos(\omega_q t) - \cos(\omega_d t)}{\omega_d^2 - \omega_q^2}\right]^2 , = |\langle X_q | v_A^2 R\rangle|^2 \left(\frac{n\pi}{L}\right)^2 \left(\frac{\omega_d}{\langle\omega\rangle}\right)^2 \times \left[\frac{\sin(\Delta\omega t/2)}{\Delta\omega}\right]^2 \sin(\langle\omega\rangle t)^2 , \quad (81)$$

where $\langle\omega\rangle = (\omega_d + \omega_q)/2$ and $\Delta\omega = (\omega_d - \omega_q)$. Equation (81) tells us that driving with a frequency ω_d close to an eigenfrequency ω_q results in a large (due to the factor $1/\Delta\omega$) kinetic energy contribution oscillating with a mean frequency $\langle\omega\rangle$. The amplitude of this oscillation is modulated with a low frequency $\Delta\omega$. This causes a beat effect in the time dependence of the kinetic energy of modes whose eigenfrequency lie close to the driving frequency: for $t < \pi/(2\Delta\omega)$, the footpoint motion pumps energy in the eigenmode, while for $\pi/(2\Delta\omega) < t < \pi/(\Delta\omega)$, this energy is extracted again and the cycle can start again. Such a beat effect was noted before (Berghmans & De Bruyne 1995) for torsional Alfvén waves and observed by Poedts & Kerner (1992) in numerical experiments. One can expect that for $\Delta\omega \to 0$, energy is pumped constantly into the eigenmode. Indeed, for driving at exactly an eigenfrequency it turns out that since

$$\frac{\sin(\Delta\omega t/2)}{\Delta\omega t/2} \to 1 \quad \text{as} \quad \frac{\Delta\omega t}{2} \to 0 ,$$

we obtain

$$E_{q,n}(t) \to \frac{t^2}{4} |\langle X_q | v_A^2 R\rangle|^2 \left(\frac{n\pi}{L}\right)^2 \times [\sin(\omega_d t)]^2 \text{ when } \omega_d \to \omega_q . \quad (82)$$

This means that driving at an eigenfrequency results in a quadratic growth of the kinetic energy contribution (and thus a linear growth of the amplitude) of the corresponding eigenmode. Modes whose eigenfrequency lie close enough to the driving frequency ($\Delta\omega < \pi/2\tau_c$) also absorb energy during the whole driving time τ_c but their growth will be slower than quadratic. The excitation of modes with $\Delta\omega > \pi/2\tau_c$ will depend on the phase in the beat period at the time $t = \tau_c$ when the driving stops. This is investigated more carefully in the following paragraph.

7.2.3. *Asymptotic Time Evolution*: $\tau_c < t \to \infty$

We again start from equation (72), taking into account that $T(t)$ vanishes for $t > \tau_c$ such that the upper limit of the integral over τ becomes now τ_c. Simple analytic integration (we forget again about the initial stage) results in

$$E_{q,n}(t) = |\langle X_q | v_A^2 R\rangle|^2 \left(\frac{n\pi}{L}\right)^2 \times \left[\omega_d \frac{\cos(\omega_q t) - \cos\omega_q(\tau_c - t)}{\omega_d^2 - \omega_q^2}\right]^2 = |\langle X_q | v_A^2 R\rangle|^2 \left(\frac{n\pi}{L}\right)^2 \left(\frac{\omega_d}{\langle\omega\rangle}\right)^2 \left[\frac{\sin(\Delta\omega\tau_c/2)}{\Delta\omega}\right]^2 \times \{\sin[\omega_q(t - \tau_c) + \langle\omega\rangle\tau_c]\}^2 , \quad (83)$$

where our previous assumption $\tau_c = m2\pi/\omega_d$ has led to considerable simplification. It can be checked that at $t = \tau_c$, equations (81) and (83) are identical. For $t > \tau_c$, the interpretation of equation (83) is straightforward: each eigenmode oscillates with its own eigenfrequency and maintains the amplitude corresponding to the phase in the beat cycle at the time the driving stopped.

As far as the influence of the time dependence of the periodic footpoint motion is concerned, we can summarize by stating that only those eigenmodes whose eigenfrequency lies within an interval $\Delta\omega = \pi/2\tau_c$ from the driving frequency ω_d are significantly excited. Whether the resulting oscillation is sustained in the loop or radiated away by the leaky modes thus depends on the relative number of leaky and body modes in this interval. In order to excite a sustained oscillation in the loop with a periodic footpoint motion, it seems therefore necessary that the driving frequency be above the eigenfrequency $\omega_b(q = 1)$ of the first body mode.

8. CONCLUSIONS AND DISCUSSION

In this paper we looked at the excitation of sausage eigenmodes by photospheric footpoint motions. Thanks to the assumed cylindrical symmetry ($m = 0$), the radial component of displacement vector (fast waves) decouples from the torsional component (Alfvén waves), which allows for a fully analytical treatment of the sausage waves in real (r, z, t)-space.

We wrote the general solution as a superposition of line-tied sausage eigenmodes $S_{q,n}$, which were identified by an equivalent Schrödinger approach as being body modes or leaky modes. The excitation of each of these sausage eigenmodes $S_{q,n}$ is determined by the time dependence of the footpoint motion (through convolution eq. [64]) and by the radial dependence of the footpoint motion (through the scalar product eq. [63]). In addition, we derived an expression for the kinetic energy contributed by each sausage eigenmode to the kinetic energy of the total sausage wave.

We then used the analytical solution for the footpoint-driven sausage wave to generate animated computer graphics in (r, z, t)-space for different types of footpoint motions. For each case, we tried to answer the following questions. What is the typical signature of the generated wave? Is wave energy being accumulated in the loop or does it leak away? What does the wave dynamics look like for $t \to \infty$?

In a first step, we looked at an impulsively driven sausage

wave as it can be generated, for example, by an exploding granule at some distance of the loop. As could be expected, we observed a spherically expanding wave front followed by a wake. This behavior is typical for waves expanding in two dimensions. When the wave front hits the loop, part of it reflects back into the ambient corona, while the rest refracts into the loop. This situation is analogous to a sideways impinging fast wave, as it has often been assumed in the literature. For the case of the sausage wave that we investigated, we found however that only 1% of the incident wave energy is captured by the loop, while the rest is reemitted again.

In a following step, we investigated the effect of the same pulse but now applied at the footpoint ($z = 0$) of the loop. It is fascinating to see the completely different behavior from the previous case. Initially, the wave front expands spherically again but when reaching the loop edge a fast outburst occurs because of the enhanced Alfvén velocity in the exterior of the loop. However, it turns out that because of the continuity imposed at the loop edge, this outburst returns back into the loop. Combined with the wave front that remains in the loop, we obtain a typical behavior as it was first derived by Pekeris (1948) for ocean waves and later used in the context of sausage waves by Roberts, Edwin, & Benz (1984). The reentry outbursting wave fronts form what has been called the periodic phase, while the wave front that propagates straight up followed by multiple reflections forms the quasi-periodic phase. Finally the Airy phase corresponds to the final decay. We think that our explanation of the formation of this typical behavior in terms of propagating wave fronts is complementary to the explanation given by Roberts, Edwin, & Benz (1984) in terms of the group velocity. Since we drive from within the loop, and a part of the perturbation that escapes from the loop reenters somewhat later, it should be no surprise that 94% of the energy is indeed permanently captured by the loop.

Finally, we considered a harmonic driving at the loop's footpoint with a single frequency ω_d. As the generated wave pattern was rather complicated, we discussed the time evolution in three stages. In the initial stage, i.e., before the perturbation reaches the other side, we observed that the wavelength of the generated wave is initially larger than expected ($2\pi/\omega_d v_A$) but later decreases down to zero. We were able to explain this behavior by making the analogy with what we learned from the pulsewise driving. In the following stage, we demonstrated, that as long as the harmonic footpoint driving goes on, interference of the driving frequency with the eigenfrequencies, causes a beat modulation in the excitation of the eigenmodes: energy is first absorbed and later reemitted. If the driving frequency coincides with a specific eigenfrequency, then the amplitude of the corresponding eigenmode grows linearly. In a last stage we looked at the resulting excitation when the driving footpoint motion has died out. Each eigenmode oscillates now with its own eigenfrequency, and its amplitude is determined by the phase it had in the beat cycle when the driving stopped. The largest excitation occurs for those eigenmodes whose eigenfrequency lies less than a distance $\Delta\omega = \pi/2\tau_c$ from the driving frequency. These modes have been absorbing energy during the whole lifetime of the footpoint motion. The fraction of the energy that is permanently captured by the loop is determined by the number of body modes within this interval. Consequently, driving the loop's feet with a frequency below the eigenfrequency of the lowest body mode results in a persisting outflow of energy into the coronal environment.

In this context, it is important to observe that the typical frequency of the photospheric motions ($\omega_d = 0.02$ rad s^{-1}; see Fig. 2.19 in Bray, Loughhead, & Durrant 1984) is much smaller than the eigenfrequency of the lowest body mode [$\omega_b(q = 1) = 1.124$ rad s^{-1} for our parameter set] and even smaller than the frequency of the lowest leaky mode [$\omega_{q=1}(n = 1) \sim \pi/\tau_A = 0.13$ rad s^{-1}, where we took $d' \to \infty$ and τ_A is the Alfvénic transit time from photosphere to photosphere]. We want to argue, however, that eigenfrequencies of coronal loops are possibly systematically overestimated by modeling the photosphere, transition region, and chromosphere as a boundary plane. Although this transition from photosphere to corona constitutes only a few percent of the total loop length, it might well be that back and forth bouncing waves spend most of their time in these transition regions because of the drastic decrease in Alfvén speed there. Taking into account this effect will strongly increase Alfvénic transit times along the loop and thus significantly decrease the eigenfrequencies.

Apart from explaining the physics of the coronal sausage wave, this case study can be a guide when studying oscillations in more realistically modeled coronal loops (e.g., by including the longitudinal dependence of the Alfvén speed) that are excited by general footpoint motions. In particular, since the sausage wave is a member of the fast waves family, our results can be a reference point for numerical studies of the "global modes" known in MHD resonant absorption theory.

The authors want to thank the anonymous referee for useful suggestions. P. D. B.'s participation was supported by the Onderzoeksfonds K. U. Leuven, OT/92/8.

REFERENCES

Athay, R. G., & White, O. R. 1978, ApJ, 226, 1135
Berghmans, D., & De Bruyne, P. 1995, ApJ, 453, 495
Bray, R. J., Loughhead, R. E., & Durrant, C. J. 1984, The Solar Granulation (Cambridge: Cambridge Univ. Press), 68
Čadež, V. M., & Ballester, J. L. 1995, A&A, 296, 550
Cally, P. S. 1986, Sol. Phys., 103, 277
Erdélyi, A., & Bateman, H. 1953, Higher Transcendental Functions, Vol. 2 (New York: McGraw-Hill)
Goossens, M., & Ruderman, M. S. 1995, Phys. Scr., T60, 171
Hollweg, J. V. 1984, ApJ, 277, 392
Morse, P. M., & Feshbach, H. 1953, Methods of Theoretical Physics (Tokyo: McGraw-Hill), 845
Pekeris, C. L. 1948, Geol. Soc. Am. Mem., 27, 117
Poedts, S., & Boyton, G. C. 1996, A&A, 306, 610
Poedts, S., & Kerner, W. 1992, J. Plasma Phys., 47, 139
Ren-Yang, Z., Sheng-Zhen, J., & Xiao-Cong, L. 1990, Sol. Phys., 130, 151
Roberts, B., Edwin, P. M., & Benz, A. O. 1984, ApJ, 29, 857
Sedláček, Z., Adam, J. A., & Roberts, B. 1986, Initial Value Problem for the 1D Wave Equation in an Inhomogeneous Plasma (Prague: Czechoslovak Acad. Sci.), Rep. IPPCZ-268
Wright, A. N., & Rickard, G. J. 1995, ApJ, 444, 458